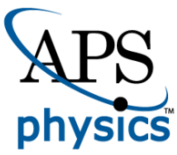

Quantal diffusion approach for multinucleon transfers in Xe + Pb collisions

S. Ayik, B. Yilmaz, O. Yilmaz, and A. S. Umar

Phys. Rev. C **100**, 014609 — Published 22 July 2019

DOI: 10.1103/PhysRevC.100.014609

Quantal diffusion approach for multi-nucleon transfers in Xe + Pb collisions

S. Ayik,[1,*] B. Yilmaz,[2] O. Yilmaz,[3] and A. S. Umar[4]

[1]*Physics Department, Tennessee Technological University, Cookeville, TN 38505, USA*
[2]*Physics Department, Faculty of Sciences, Ankara University, 06100 Ankara, Turkey*
[3]*Physics Department, Middle East Technical University, 06800 Ankara, Turkey*
[4]*Department of Physics and Astronomy, Vanderbilt University, Nashville, TN 37235, USA*

(Dated: June 11, 2019)

Employing a quantal diffusion description based on the stochastic mean-field (SMF) approach, we analyze the mass distribution of the primary fragments in the collisions of ^{136}Xe + ^{208}Pb system at the bombarding energy $E_{\rm c.m.} = 526$ MeV. This quantal approach provides a good description of the primary fragment distribution without any adjustable parameter, including the effects of shell structure.

I. INTRODUCTION

It has been recognized that multi-nucleon transfer in heavy-ion collisions provide a suitable mechanism for synthesizing new neutron rich nuclei [1–3]. In particular, multi-nucleon transfer in heavy-ion collisions involving heavy projectile-target combinations could be utilized for the production of new neutron rich heavy nuclei [4–6]. For this purpose, experimental investigations have been carried out for heavy-ion collisions with heavy projectile-target combinations at near barrier energies [7–9]. Collisions of heavy systems at near barrier energies predominantly lead to dissipative deep-inelastic reactions and quasi-fission reactions. In dissipative collisions large part of the bombarding energy is converted into internal excitations, and the multi-nucleon transfer occurs between the projectile and target nuclei. Recently, the multi-nucleon transfer mechanism has been investigated for the reaction ^{136}Xe + ^{208}Pb at bombarding energies $E_{\rm c.m.} = 423$, 526, and 617 MeV, and di-nuclear mass distributions of the primary fragments have been measured [7]. This system has two unique properties: (i) the neutron shells in the projectile xenon, $N = 82$, and the target lead, $N = 126$, are closed, and (ii) the $Q_{gg}-$value distributions for nucleon transfers that drive the system toward symmetry and also toward asymmetry have negative values. As a result, the identity of the projectile and target are strongly maintained but data exhibits a broad mass distribution around the projectile and the target masses.

The multi-dimensional phenomenological Langevin type dynamical approach [4,5,10,11] is quite successful in reproducing many aspects of the data, but the approach is semi-classical and involves a set of adjustable parameters. The mean-field approach of the time-dependent Hartree-Fock (TDHF) theory provides a microscopic approach for describing heavy-ion reaction mechanism at low bombarding energies [12–14]. Since several years, the TDHF approach has been used for describing the quasi-fission reactions [15–20]. While the mean-field theory provides a good description for the average values of the collective motion it is not able to accurately describe dynamics of fluctuations for this motion. The fragment mass distributions provide a good example for the shortcoming of the mean-field description. The TDHF calculations give nearly zero drift for the mass asymmetry, while the dominant aspect of the data is a broad mass distributions around the projectile and target masses resulting from multi-nucleon diffusion mechanism. The description of such large fluctuations requires an approach beyond the mean-field theory. The time-dependent random phase approximation (TDRPA) approach of Balian and Vénéroni [21–25] provides a possible approach for calculating dispersion of fragment mass distributions. However, this approach has severe technical difficulties in applications to the collisions of asymmetric systems [26]. Here, we employ the stochastic mean-field (SMF) approach [27,28] to calculate the mass distribution of the primary fragments in ^{136}Xe + ^{208}Pb system. In Sec. II, we present a brief description of the quantal nucleon diffusion mechanism based on the SMF approach. In Sec. III, we present an analysis of the potential energy surface in the vicinity of the ^{136}Xe + ^{208}Pb system. The result of calculations for the mass distribution in ^{136}Xe + ^{208}Pb collisions is reported in Sec. IV, and conclusions are given in Sec. V.

II. QUANTAL NUCLEON DIFFUSION MECHANISM

In the SMF approach the collision dynamics is described in terms of an ensemble of mean-field events. The single-particle density matrix of each event, $\rho^{\lambda}(\vec{r},\vec{p},t)$, is determined by the self-consistent mean-field of the corresponding event. Here λ indicates the event label. The ensemble is considered to be generated by incorporating the quantal and thermal fluctuations at the initial state. The elements of the initial density matrix are specified by uncorrelated random Gaussian distributions with the average values specified by the mean occupation numbers and the second moments are determined by Eq. (3) given below. In terms of the ensemble of mean-field events, it is possible to calculate not only the mean values, but the entire probability distributions of one-body observables. When a di-nuclear structure is maintained during the collision, such as deep inelastic and quasi-fission reactions, we do not need to generate such an ensemble of mean-field events. In this case it is possible to describe the collision dynamics, in a much simpler manner, in terms of a few relevant macroscopic variables, such as mass and charge asymmetry, the relative linear momentum and the orbital angular momentum. In di-nuclear geometry, it is possible to define these macroscopic

* ayik@tntech.edu

variables in terms of the TDHF solutions with the help of window dynamics. The SMF approach gives rise to Langevin type transport description including quantal shell effects for the macroscopic variables [29,30]. It is possible to calculate transport coefficients associate with the macroscopic variables in terms of the ordinary TDHF solutions. For the details of the SMF approach and the applications we refer the reader to the previous publications [31–33]. Here, we consider nucleon exchange in collisions between heavy nuclei at near barrier energies in which the di-nuclear structure is maintained. We take the neutron N_1^λ and proton Z_1^λ numbers of the projectile-like fragments as the macroscopic variables. In each event λ, the neutron and proton numbers are determined by integrating the nucleon density over the projectile side of the window between the colliding nuclei,

$$\begin{pmatrix} N_1^\lambda(t) \\ Z_1^\lambda(t) \end{pmatrix} = \int d^3r\,\Theta\left[x'(t)\right] \begin{pmatrix} \rho_n^\lambda(\vec{r},t) \\ \rho_p^\lambda(\vec{r},t) \end{pmatrix} \tag{1}$$

where $x'(t) = [y - y_0(0)]\sin\theta(t) + [x - x_0(t)]\cos\theta(t)$. The $(x,y)-$plane represents the reaction plane, with $x-$axis being the beam direction in the center of mass frame (COM) of the colliding ions. The window plane is perpendicular to the inter-nuclear axis and its orientation is specified by the condition $x'(t) = 0$. In this expression, $x_0(t)$ and $y_0(t)$ denote the coordinates of the window center relative to the origin of the COM frame, $\theta(t)$ is the smaller angle between the orientation of the inter-nuclear axis and the beam direction. For each impact parameter b or the initial orbital angular momentum, as described in Appendix A of Ref. [32], by employing the TDHF description, it is possible to determine time evolution of the rotation angle $\theta(t)$ of the inter-nuclear axis. The coordinates $x_0(t)$ and $y_0(t)$ of the center point of the window are located at the center of the minimum density slice on the neck between the colliding ions. As an example, Fig. 1 shows the collision geometry in the ^{136}Xe + ^{208}Pb system at $E_{\rm c.m.} = 526$ MeV with the initial orbital angular momentum $\ell = 100\hbar$ at times $t = 300$ fm/c , $t = 600$ fm/c and $t = 900$ fm/c. The window plane and inter-nuclear axis of the di-nuclear complex are indicated by thick and dash lines in frame (b) of this figure. In the following, all quantities are calculated for a given initial orbital angular momentum ℓ, but for the purpose of clarity of expressions, we do not attach the angular momentum label to the quantities. The quantity in Eq. (1)

$$\rho_\alpha^\lambda(\vec{r},t) = \sum_{ij\in\alpha} \Phi_j^{*\alpha}(\vec{r},t;\lambda)\rho_{ji}^\lambda\Phi_i^\alpha(\vec{r},t;\lambda)\,, \tag{2}$$

denotes the neutron and proton number densities in the event λ of the ensemble of single-particle density matrices. Here and in the rest of the article, we use the notation $\alpha = n, p$ for the proton and neutron labels. According to the main postulate of the SMF approach, the elements of the initial density matrix have uncorrelated Gaussian distributions with the zero mean values $\bar{\rho}_{ji}^\lambda = \delta_{ji}n_j$ and the second moments determined by,

$$\overline{\delta\rho_{ji}^\lambda\delta\rho_{i'j'}^\lambda} = \frac{1}{2}\delta_{ii'}\delta_{jj'}\left[n_i(1-n_j) + n_j(1-n_i)\right]\,, \tag{3}$$

where n_j are the average occupation numbers of the single-particle wave functions of the initial state. At zero initial temperature, the occupation numbers are zero or one, at finite initial temperatures the occupation numbers are given by the Fermi-Dirac functions. Here and below, the bar over the quantity indicates the average over the generated ensemble.

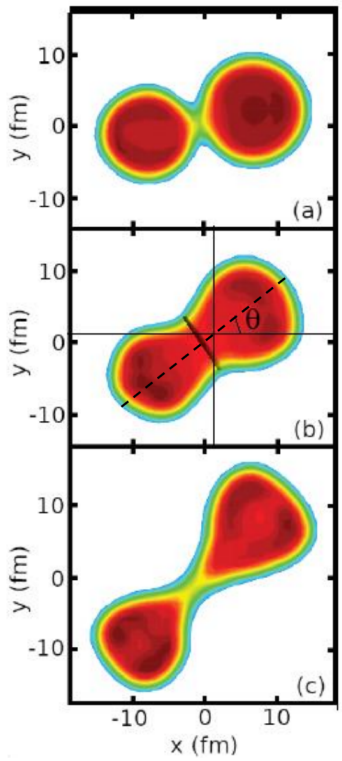

FIG. 1. (color online) The density profile and the collision geometry of the ^{136}Xe + ^{208}Pb collisions at $E_{\rm c.m.} = 526$ MeV with the initial orbital angular momentum $\ell = 100\hbar$ at times (a) $t = 300$ fm/c, (b) $t = 600$ fm/c, and (c) $t = 900$ fm/c.

Below, we briefly discuss the derivation of the Langevin equation for neutron and proton numbers of the projectile-like fragments, and for details we refer to Refs. [31,32]. The rate of change of the neutron and the proton numbers for the projectile-like fragment are given by,

$$\frac{d}{dt}\begin{pmatrix} N_1^\lambda(t) \\ Z_1^\lambda(t) \end{pmatrix} = \int d^3r\,\Theta(x')\frac{\partial}{\partial t}\begin{pmatrix} \rho_n^\lambda(\vec{r},t) \\ \rho_p^\lambda(\vec{r},t) \end{pmatrix}\,. \tag{4}$$

In this expression, we neglected the terms determined by the rate of change of the position and rotation of the window plane, since tangential and linear velocities of the window are much smaller than the Fermi velocity of nucleons. Using the continuity equation, we obtain a Langevin description for stochastic evolution the neutron and proton numbers of the projectile-like fragments

$$\begin{aligned}\frac{d}{dt}\begin{pmatrix} N_1^\lambda(t) \\ Z_1^\lambda(t) \end{pmatrix} &= \int d^3r\,g(x')\begin{pmatrix} \hat{e}\cdot\vec{j}_n^\lambda(\vec{r},t) \\ \hat{e}\cdot\vec{j}_p^\lambda(\vec{r},t) \end{pmatrix} \\ &= \begin{pmatrix} v_n^\lambda(t) \\ v_p^\lambda(t) \end{pmatrix}\,,\end{aligned} \tag{5}$$

where $\hat{e}$ denotes the unit vector along the inter-nuclear axis with components $\hat{e}_x = \cos\theta$ and $\hat{e}_y = \sin\theta$. The quantity $g(x) = \left(1/\kappa\sqrt{2\pi}\right)\exp\left(-x^2/2\kappa^2\right)$ represents a Gaussian with a dispersion κ, which behaves almost like delta function for sufficiently small κ. In the numerical calculations dispersion of the Gaussian is taken to be on the order of the lattice size $\kappa = 1.0$ fm. The right side of Eq. (5) defines the fluctuating drift coefficients $v_\alpha^\lambda(t)$ for the neutrons and the protons in the event λ. In the SMF approach the fluctuating current density vector in the event λ is given by,

$$\vec{j}_\alpha^\lambda(\vec{r},t) = \frac{\hbar}{m}\sum_{ij\in\alpha} Im\left(\Phi_j^{*\alpha}(\vec{r},t;\lambda)\vec{\nabla}\Phi_i^\alpha(\vec{r},t;\lambda)\rho_{ji}^\lambda\right) . \quad (6)$$

A. TDHF calculations for mean dynamical path

Equations for the mean values of proton $Z_1(t) = \bar{Z}_1^\lambda(t)$ and neutron $N_1(t) = \bar{N}_1^\lambda(t)$ numbers of the projectile-like fragments are obtained by taking the ensemble averaging of the Langevin Eq. (5). For small amplitude fluctuations, and using the fact that average values of density matrix elements are given by the average occupation numbers as $\bar{\rho}_{ji}^\lambda = \delta_{ji}n_j$, we obtain the usual mean-field results given by the TDHF equations,

$$\frac{d}{dt}\begin{pmatrix} N_1(t) \\ Z_1(t)\end{pmatrix} = \int d^3r\, g(x')\begin{pmatrix} \hat{e}\cdot\vec{j}_n(\vec{r},t) \\ \hat{e}\cdot\vec{j}_p(\vec{r},t)\end{pmatrix} = \begin{pmatrix} v_n(t) \\ v_p(t)\end{pmatrix}. \quad (7)$$

Here, the mean values of the densities and the currents densities of neutron and protons are given by,

$$\rho_\alpha(\vec{r},t) = \sum_{h\in\alpha}\Phi_h^{*\alpha}(\vec{r},t)\Phi_h^\alpha(\vec{r},t) \quad (8)$$

and

$$\vec{j}_\alpha(\vec{r},t) = \frac{\hbar}{m}\sum_{h\in\alpha}\mathrm{Im}\left(\Phi_h^{*\alpha}(\vec{r},t)\vec{\nabla}\Phi_h^\alpha(\vec{r},t)\right) , \quad (9)$$

where the summation h runs over the occupied states originating both from the projectile and the target nuclei. The drift coefficients $v_p(t)$ and $v_n(t)$ denote the net proton and neutron currents across the window.

We carry out TDHF calculations for $^{136}\mathrm{Xe} + {}^{208}\mathrm{Pb}$ at $E_{\mathrm{c.m.}} = 526$ MeV for a set initial orbital angular momenta in the range $\ell = (100-300)\,\hbar$. This range of the orbital angular momenta correspond to the data collection range in the laboratory frame [7]. Table I shows the result of TDHF calculations for the primary values of mass and charge of the projectile-like and target-like fragments, the final orbital angular momenta, the total kinetic energy, the center of mass and laboratory scattering angles, and the total excitation energy for a set initial orbital angular momenta. These calculations and calculations presented in the rest of the paper are performed using the TDHF program developed by Umar *et al.* [34]. A large part of the initial kinetic energy is dissipated during the collisions. The calculations give very small amount of mass drift, on the order of one mass unit of neutron and proton drifts at all impact parameters, which is consistent with data. As a result of the neutron shell closures in both projectile and target with $N_0 = 82$ and $N_0 = 126$, and the due to $Q_{gg}-$ values, the $^{136}\mathrm{Xe} + {}^{208}\mathrm{Pb}$ di-nuclear system occupies a local potential minimum state in the (N-Z) plane. The system has a unique aspect of strongly preserving its initial di-nuclear structure on the average, but data exhibits remarkably broad mass distribution of the primary fragments.

TABLE I. Result of TDHF calculations for $^{136}\mathrm{Xe} + {}^{208}\mathrm{Pb}$ at $E_{\mathrm{c.m.}} =$ 526 MeV for primary values of mass and charge of the projectile-like (A_1^f, Z_1^f) and target-like fragments (A_2^f, Z_2^f), final orbital angular momentum ℓ_f, total kinetic energy (TKE), center of mass $\theta_{\mathrm{c.m.}}$, laboratory scattering angles (θ_1^{lab},θ_2^{lab}), and total excitation energy E^* for a set initial orbital angular momentum ℓ_i.

$\ell_i(\hbar)$	A_1^f	Z_1^f	A_2^f	Z_2^f	$\ell_f(\hbar)$	TKE (MeV)	$\theta_{c.m.}$	E^* (MeV)	θ_1^{lab}	θ_2^{lab}
100	135	53.6	209	82.4	83.1	346	125	185	74.8	24.2
120	135	53.9	209	82.1	101	349	116	181	67.8	28.5
140	137	54.4	207	81.6	119	350	116	179	61.6	32.5
160	138	55.2	206	80.8	131	353	97.9	176	55.8	36.5
180	139	55.5	205	80.5	146	355	90.5	172	55.7	36.6
200	137	54.9	207	81.1	166	348	81.3	179	47.5	41.6
220	137	54.8	207	81.2	177	350	80.8	176	45.6	43.0
240	138	55.6	206	80.4	192	367	79.5	160	45.2	44.6
260	137	55.1	207	80.9	213	397	79.1	128	46.1	45.8
280	136	54.8	208	81.2	238	429	78.4	103	46.6	47.3
300	137	54.6	207	81.4	277	472	77.9	53.7	47.3	49.2

B. Quantal Langevin equation for neutron and proton diffusion

Equation (5) provides a Langevin description for the stochastic evolution the neutron and the proton numbers of the projectile-like fragments. For relatively small fluctuations, we linearize the Langevin equation around the mean evolution. The drift coefficients $v_\alpha^\lambda(t)$ fluctuate from event to event due to stochastic elements of the initial density matrix $\delta\rho_{ji}^\lambda$ and due to the different sets of the wave functions in different events. We can represent the fluctuations due to state dependence of the drift coefficients in terms of the fluctuating neutron and proton numbers as $v_\alpha(N_1^\lambda, Z_1^\lambda)$. As a result, we can express the linearized Langevin equation as,

$$\frac{d}{dt}\begin{pmatrix}\delta Z_1(t)\\ \delta N_1(t)\end{pmatrix} = \begin{pmatrix}\frac{\partial v_p}{\partial Z_1}\left(Z_1^\lambda - Z_1\right) + \frac{\partial v_p}{\partial N_1}\left(N_1^\lambda - N_1\right)\\ \frac{\partial v_n}{\partial Z_1}\left(Z_1^\lambda - Z_1\right) + \frac{\partial v_n}{\partial N_1}\left(N_1^\lambda - N_1\right)\end{pmatrix} + \begin{pmatrix}\delta v_p^\lambda(t)\\ \delta v_n^\lambda(t)\end{pmatrix} , \quad (10)$$

where the derivatives of drift coefficients are evaluated at the mean values N_1 and Z_1. The linear limit provides a good approximation for small amplitude fluctuations and it becomes even better if the fluctuations are nearly harmonic around the

mean values. The stochastic part $\delta v_\alpha^\lambda(t)$ of drift coefficients are given by,

$$\delta v_\alpha^\lambda(t) = \frac{\hbar}{m}\sum_{ij\in\alpha}\int d^3r g(x') \times \mathrm{Im}\left(\Phi_j^{*\alpha}(\vec{r},t)\,\widehat{e}\cdot\vec{\nabla}\Phi_i^\alpha(\vec{r},t)\delta\rho_{ji}^\lambda\right) . \quad (11)$$

The variances and the co-variance of neutron and proton distribution are defined as $\sigma_{NN}^2(t) = \overline{\left(N_1^\lambda - N_1\right)^2}$, $\sigma_{ZZ}^2(t) = \overline{\left(Z_1^\lambda - Z_1\right)^2}$, and $\sigma_{NZ}^2(t) = \overline{\left(N_1^\lambda - N_1\right)\left(Z_1^\lambda - Z_1\right)}$. Multiplying both side of Langevin Eqs. (10) by $N_1^\lambda - N_1$ and $Z_1^\lambda - Z_1$, and taking the ensemble average, we find evolution of the covariances are specified by the following set of coupled differential equations [35,36],

$$\frac{\partial}{\partial t}\sigma_{NN}^2 = 2\frac{\partial v_n}{\partial N_1}\sigma_{NN}^2 + 2\frac{\partial v_n}{\partial Z_1}\sigma_{NZ}^2 + 2D_{NN} \quad (12)$$

$$\frac{\partial}{\partial t}\sigma_{ZZ}^2 = 2\frac{\partial v_p}{\partial Z_1}\sigma_{ZZ}^2 + 2\frac{\partial v_p}{\partial N_1}\sigma_{NZ}^2 + 2D_{ZZ} \quad (13)$$

$$\frac{\partial}{\partial t}\sigma_{NZ}^2 = \frac{\partial v_p}{\partial N_1}\sigma_{NN}^2 + \frac{\partial v_n}{\partial Z_1}\sigma_{ZZ}^2 + \sigma_{NZ}^2\left(\frac{\partial v_p}{\partial Z_1} + \frac{\partial v_n}{\partial N_1}\right). \quad (14)$$

In these expressions D_{NN} and D_{ZZ} denote the neutron and proton quantal diffusion coefficients which are discussed below. It is well known that the Langevin equation (10) is equivalent to the Fokker-Planck equation for the correlated distribution function $P(N,Z)$ of the neutron and proton numbers of projectile-like or target-like fragments [37]. Here, we consider the mass number distribution of the projectile-like and target-like primary fragments. Analytic solution of the Langevin equation for the projectile-like fragments is given by a Gaussian function $P(A,t)$

$$P(A) = \frac{1}{\sqrt{2\pi}\sigma_{AA}}\exp\left[-\frac{1}{2}\left(\frac{A-A_1}{\sigma_{AA}}\right)^2\right], \quad (15)$$

where $A_1 = N_1 + Z_1$ is the mean value of the mass number of the projectile-like fragments and the variance is given by $\sigma_{AA}^2 = \sigma_{NN}^2 + \sigma_{ZZ}^2 + 2\sigma_{NZ}^2$. Distribution function of the target-like fragments is given by a similar expression. We should note that the single Gaussian solution for Fokker-Planck equation and hence the Langevin equation is valid when the derivatives of drift coefficients are continuous as approached from left and right of the mean neutron and proton numbers. If the derivative of drift coefficients are discontinuous, which is the case in the ^{136}Xe + ^{208}Pb system, the mass dispersion in the asymmetric direction $\sigma_{AA}^<$ and the symmetric direction $\sigma_{AA}^>$ have different values, therefore we cannot represent the solution of the Langevin Eq. (10) by a single Gaussian distribution. In this case, as it is discussed in Sec. III, it is possible to represent the solutions of the Langevin equation as a suitable combination of Gaussian distributions toward asymmetry $P^<(A)$ and toward symmetry $P^>(A)$.

C. Neutron and proton diffusion coefficients

The quantal expression of the diffusion coefficients for neutron and proton transfers are determined by the autocorrelation functions of the stochastic part of the drift coefficients as [31–33],

$$\int_0^t dt' \overline{\delta v_\alpha^\lambda(t)\delta v_\alpha^\lambda(t')} = D_{\alpha\alpha}(t) . \quad (16)$$

We refer the reader to Refs. [31,32] in which a detail evaluation of the autocorrelation functions are presented. Here, for completeness of the presentation, we give the results. The quantal expressions of the proton and neutron diffusion coefficients take the form,

$$D_{\alpha\alpha}(t) = \int_0^t d\tau\int d^3r\tilde{g}(x')\left(G_T(\tau)J_{\perp,\alpha}^T(\vec{r},t-\tau/2) + G_P(\tau)J_{\perp,\alpha}^P(\vec{r},t-\tau/2)\right) - \int_0^t d\tau\,\mathrm{Re}\left(\sum_{h'\in P,h\in T}A_{h'h}^\alpha(t)A_{h'h}^{*\alpha}(t-\tau) + \sum_{h'\in T,h\in P}A_{h'h}^\alpha(t)A_{h'h}^{*\alpha}(t-\tau)\right) , \quad (17)$$

where $J_{\perp,\alpha}^T(\vec{r},t-\tau/2)$ represents the sum of the magnitude of current densities perpendicular to the window due to the hole wave functions originating from target,

$$J_{\perp,\alpha}^T(\vec{r},t-\tau/2) = \frac{\hbar}{m}\sum_{h\in T}|\mathrm{Im}\Phi_h^{*\alpha}(\vec{r},t-\tau/2) \times\left(\hat{e}\cdot\vec{\nabla}\Phi_h^\alpha(\vec{r},t-\tau/2)\right)| , \quad (18)$$

and $J_{\perp,\alpha}^P(\vec{r},t-\tau/2)$ is given by a similar expression in terms of the hole wave functions originating from the projectile. We observe that there is a close analogy between the quantal expression and the classical diffusion coefficient for the random walk problem [29,30]. The first line in the quantal expression gives the sum of the nucleon currents across the window from the target-like fragment to the projectile-like fragment and from the projectile-like fragment to the target-like fragment, which is integrated over the memory. This is analogous to the random walk problem, in which the diffusion coefficient is given by the sum of the rate for the forward and backward steps. The second line in the quantal diffusion expression stands for the Pauli blocking effects in nucleon transfer mechanism, which does not have a classical counterpart. The quantities in the Pauli blocking factors are determined by

$$A_{h'h}^\alpha(t) = \frac{\hbar}{2m}\int d^3r g(x')\left(\Phi_{h'}^{*\alpha}(\vec{r},t)\hat{e}\cdot\vec{\nabla}\Phi_h^\alpha(\vec{r},t) - \Phi_h^\alpha(\vec{r},t)\hat{e}\cdot\vec{\nabla}\Phi_{h'}^{*\alpha}(\vec{r},t)\right) . \quad (19)$$

The memory kernel $G_T(\tau)$ in Eq. (19) is given by

$$G_T(\tau) = \frac{1}{\sqrt{4\pi}}\frac{1}{\tau_T}\exp[-(\tau/2\tau_T)^2] , \quad (20)$$

with the memory time determined by the average flow velocity u_T of the target nucleons across the window according to $\tau_T = \kappa/|u_T(t)|$, and $G_P(\tau)$ is given by a similar expression. In a previous work, we estimated the memory time to be about $\tau_T = \tau_P \approx 25$ fm/c, which is much shorter than the contact time of about 600 fm/c [32]. As a result the memory effect is not important for the nucleon diffusion mechanism. We note that the quantal diffusion coefficients are entirely determined in terms of the occupied single-particle wave functions obtained from the TDHF solutions. According to the non-equilibrium fluctuation-dissipation theorem, the fluctuation properties of the relevant macroscopic variables must be related to the mean properties. Consequently, evaluations of diffusion coefficients in terms of mean-field properties is not surprising. As examples, Fig. 2 shows neutron (a) and proton (b) diffusion coefficients for the ^{136}Xe + ^{208}Pb system at $E_{\rm c.m.} = 526$ MeV for the initial orbital angular momenta $\ell = 100\hbar$, $\ell = 160\hbar$, and $\ell = 200\hbar$, as function of time.

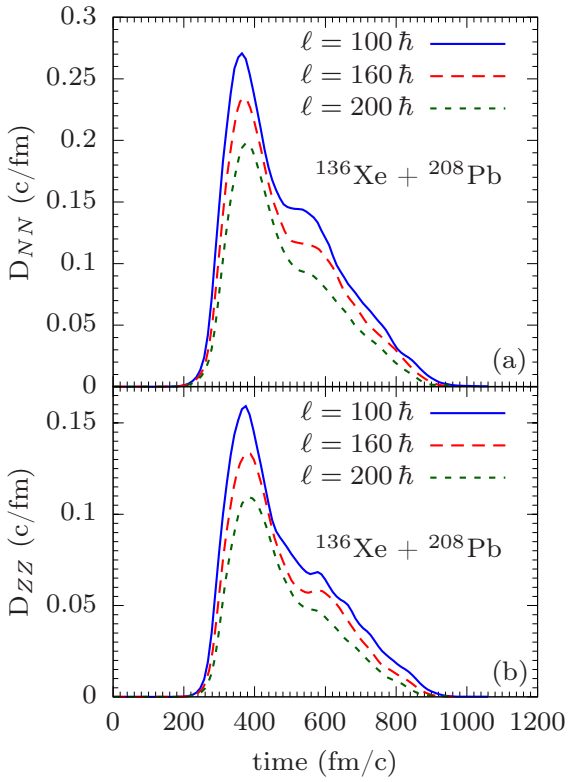

FIG. 2. (color online) The neutron (a) and proton (b) diffusion coefficients as a function of time for the ^{136}Xe + ^{208}Pb collisions at $E_{\rm c.m.} = 526$ MeV with the initial orbital angular momenta $\ell = 100\hbar$, $\ell = 160\hbar$, and $\ell = 200\hbar$.

III. POTENTIAL ENERGY SURFACE IN N-Z PLANE

For solutions of the co-variances from Eqs. (12-14), in addition to the diffusion coefficients D_{NN} and D_{ZZ}, we need to know the rate of change of the drift coefficients. In the ^{136}Xe + ^{208}Pb system both projectile and target have neutron close shells with $N = 82$ and $N = 126$, respectively. Furthermore, this di-nuclear system is placed at the bottom of a local minimum in the potential energy surface. This is evident from the negative $Q_{gg}-$value distribution of the di-nuclear systems in vicinity of ^{136}Xe + ^{208}Pb . As seen from Fig. 1 of Ref. [7], Q_{gg}-values take increasingly negative values for drifts toward asymmetry, and smaller negative values for drifts toward symmetry. As a result, the system does not exhibit any visible drift between the mass numbers of projectile and target nuclei, but the potential energy surface in (N,Z) plane has a strong influence on the nucleon diffusion mechanism. We consider the projectile-like fragments and indicate the position of local equilibrium by the neutron and proton numbers of the projectile, $N_0 = 82$ and $Z_0 = 54$ on the (N,Z) plane in Fig. 3. The Einstein relation provides a very useful relation between the potential energy surface and drift coefficients, as we discuss below. In order to employ this relation we need extract information from the TDHF calculations about the potential energy surface in the neighborhood of the minimum position, where ^{136}Xe is located. The potential energy is most conveniently expressed in terms of distances from the equilibrium position along the iso-scalar and iso-vector drift paths. The charge asymmetry of the projectile ^{136}Xe is $(78-52)/136 = 0.206$. The set of nuclei which have the approximately the same charge asymmetry values are represented by thick dash-line following thick solid line (blue line in color) in Fig. 3. We refer to this line as the iso-scalar drift path. The angle between iso-scalar path and neutron axis is about $\phi = 30^\circ$, which indicates the iso-scalar line is extending nearly alone the beta stability valley in vicinity of the projectile-like fragments and similarly in the vicinity of target-like fragments. In Fig. 3, thick dash-line following thick solid line (red line in color), which is perpendicular to the iso-scalar path, is referred as the iso-vector drift path. We represent the potential energy surface in $(N,Z)-$plane in terms of two parabolic forms in the iso-scalar and in the iso-vector directions centered at the local equilibrium position of projectile ^{136}Xe as,

$$U(N_1,Z_1) = \frac{1}{2}b\,(n\cos\phi - z\sin\phi)^2 + \frac{1}{2}a\,(n\sin\phi + z\cos\phi)^2 \ . \qquad (21)$$

Here $n = N_0 - N_1$ and $z = Z_1 - Z_0$, and (N_1,Z_1) indicate neutron and proton number of a projectile-like fragment in vicinity of (N_0,Z_0). As seen from Fig. 1 in Ref. [7], $Q_{gg}-$values for nucleon exchanges has a asymmetric distribution, become increasingly negative toward asymmetry, and take smaller negative values toward symmetry. As a result, the parabolic shape of the potential energy, particularly in the iso-scalar direction, can not have a symmetric form. Only for the purpose of clarity we represent the potential parabolas in the symmetric form in Eq. (21). However, in particular in the iso-scalar direction, the parabolic form of the potential energy must have an asymmetric shape. It must have a larger curvature in the asymmetry direction than the curvature in the symmetry direction. The situation is analogous to the elastic potential energy of an asymmetric spring.

In order to determine the curvature parameters, we employ

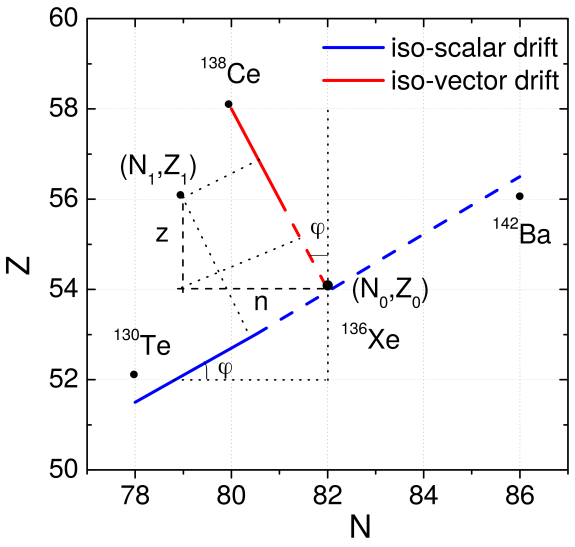

FIG. 3. (color online) Iso-scalar (thick solid and dash blue line) and iso-vector drift (thick solid and dash red line) paths in the (N,Z)-plane. The locations of ^{136}Xe, ^{138}Ce, ^{130}Te and ^{142}Ba are indicated by black dots.

the Einstein's relation, which provides a relation between the diffusion and drift coefficients in the transport mechanism of the relevant collective variables and it is often used in the phenomenological approaches [29,30,35,36]. According to the Einstein's relation, the connection between the neutron $v_n(t)$ and proton $v_p(t)$ drift coefficients and the corresponding diffusion coefficients are given by,

$$v_n(t) = -\frac{D_{NN}}{T}\frac{\partial U}{\partial N_1} = D_{NN}\left(\beta R_v(t)\cos\phi + \alpha R_s(t)\sin\phi\right) \quad (22)$$

and

$$v_p(t) = -\frac{D_{ZZ}}{T}\frac{\partial U}{\partial Z_1} = D_{ZZ}\left(\beta R_v(t)\sin\phi - \alpha R_s(t)\cos\phi\right) . \quad (23)$$

Here, the temperature is absorbed into the curvature parameters $\beta = b/T$, $\alpha = a/T$, and the quantities $R_v(t) = n\cos\phi - z\sin\phi$, $R_s(t) = n\sin\phi + z\cos\phi$ represent the distances of an arbitrary fragment (N_1,Z_1) located in the vicinity of the projectile from the iso-vector and the iso-scalar lines, respectively. Because of the analytical form, we can readily calculate the derivatives of the drift coefficients to give,

$$\partial v_n(t)/\partial N_1 = -D_{NN}\left(\beta\cos^2\phi + \alpha\sin^2\phi\right), \quad (24)$$
$$\partial v_n(t)/\partial Z_1 = +D_{NN}\left(\alpha-\beta\right)\cos\phi\sin\phi, \quad (25)$$
$$\partial v_p(t)/\partial Z_1 = -D_{ZZ}\left(\beta\sin^2\phi + \alpha\cos^2\phi\right), \quad (26)$$
$$\partial v_p(t)/\partial N_1 = +D_{ZZ}\left(\alpha-\beta\right)\cos\phi\sin\phi . \quad (27)$$

In principle, it is possible to determine the curvature parameters and hence the derivatives of the drift coefficients from the mean-drift path calculated in the TDHF approach. However, this does not work in the collision of the ^{136}Xe + ^{208}Pb system. The mean values of neutron and proton numbers of projectile-like fragments $(N_1 \approx N_0, Z_1 \approx Z_0)$ are nearly equal to their initial values, and similarly for the projectile-like fragments. Therefore, Eqs. (22,23) do not allow to determine the curvature parameters from drift information of the system.

A. Curvature parameters for the potential energy parabola

For determining the curvature parameters, we choose two nearby systems ^{130}Te + ^{214}Po and ^{138}Ce + ^{206}Pt. The total mass numbers of both systems equal to the total mass number of ^{136}Xe + ^{208}Pb. The neutron number and proton number of ^{130}Te are smaller than ^{136}Xe by four units and two units, respectively. It has a charge asymmetry of 0.200, which is nearly the same as for the ^{136}Xe, and as a result it is located very near to the iso-scalar line as indicated in Fig. 3. On the other hand, in ^{138}Ce the neutron number is smaller by two units and proton number is larger by four units than ^{136}Xe, and it is located on the iso-vector line as indicated in Fig. 3. We carry out the SMF calculations for the ^{130}Te + ^{214}Po and the ^{138}Ce + ^{206}Pt at the same $E_{\rm c.m.} = 526$ MeV and for the initial orbital angular momentum $\ell = 100\hbar$.

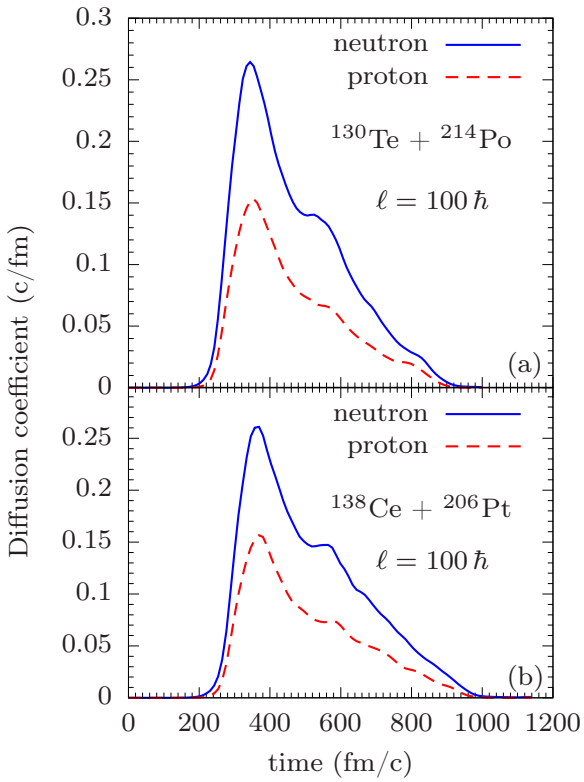

FIG. 4. (color online) The neutron and proton diffusion coefficients as a function of time for the ^{130}Te + ^{214}Po (a) and for the ^{138}Ce + ^{206}Pt (b) collisions at the $E_{\rm c.m.} = 526$ MeV with the initial orbital angular momentum $\ell = 100\hbar$.

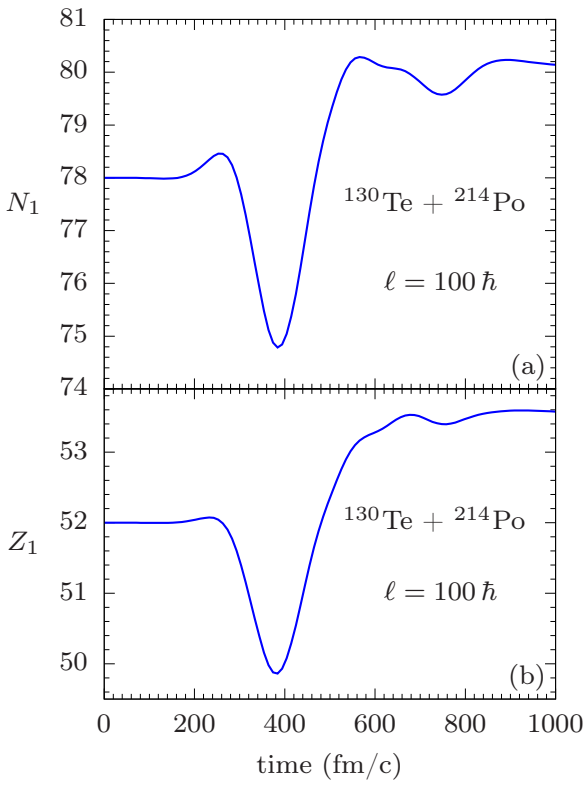

FIG. 5. (color online) The neutron (a) and proton (b) drift paths of the projectile-like fragments as a function of time for the $^{130}\mathrm{Te}+^{214}\mathrm{Po}$ collisions with the $E_{\mathrm{c.m.}} = 526$ MeV at the initial orbital angular momentum $\ell = 100\,\hbar$.

Figure 4 shows the neutron and proton diffusion coefficients for the $^{130}\mathrm{Te}+^{214}\mathrm{Po}$ system (a) and the $^{138}\mathrm{Ce}+^{206}\mathrm{Pt}$ system (b) at $E_{\mathrm{c.m.}} = 526$ MeV and orbital angular momentum $\ell = 100\,\hbar$. In these collisions the contact starts at 200 fm/c, fragments separate at around 800 fm/c. In the TDHF description, the potential energy surface involves the full effect of the shell structure and therefore has a complex shape. Figure 5 shows the result of the TDHF calculations of the mean values of the neutron and proton numbers of the projectile-like fragments as a function of time for $^{130}\mathrm{Te}+^{214}\mathrm{Po}$. The system initially drifts toward asymmetry along the iso-scalar line until about 400 fm/c. As the system heats up the shell effects disappear, the system reverses direction, drifts along the symmetry towards the local minimum and before reaching the minimum location of ^{136}Xe, it breaks up. By eliminating α from Eq. (22) and Eq. (23), we can derive an expression for β in terms of drift and diffusion coefficients. We use the drift information of $^{130}\mathrm{Te}+^{214}\mathrm{Po}$ to determine the average value of the iso-scalar curvature parameter toward asymmetry direction $\beta_<$ in the time interval from $t_1 = 480$ fm/c to $t_2 = 540$ fm/c. This interval is indicated by thick blue line on the iso-scalar drift path in Fig. 3, and it approximately corresponds to the average taken over maximum overlap of the colliding nuclei during the iso-scalar drift. In this manner, we estimate the average value of the curvature parameter in the asymmetric side of the of ^{136}Xe along the iso-scalar path as,

$$\beta_< = \frac{1}{\Delta t}\int_{t_1}^{t_2} d\tau \frac{1}{R_v(\tau)}\left(\frac{v_n(\tau)}{D_{NN}(\tau)}\cos\phi + \frac{v_p(\tau)}{D_{ZZ}(\tau)}\sin\phi\right) = 0.127\,. \quad (28)$$

Here, $\Delta t = t_2 - t_1$ and distance R_v is evaluated with $N_1(t), Z_1(t)$ on the iso-scalar path. The drift coefficients are determined from rate of change of the neutron and proton numbers $v_n = \partial N_1/\partial t$ and $v_p = \partial Z_1/\partial t$ in Fig. 5.

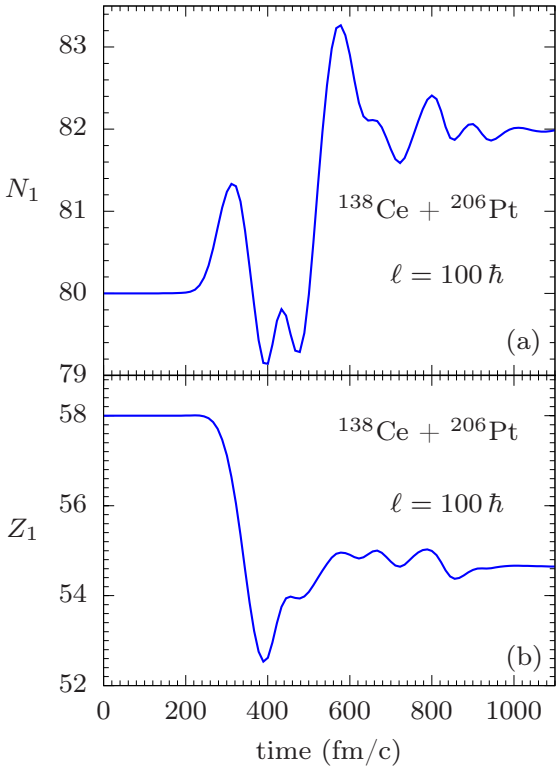

FIG. 6. (color online) The neutron (a) and proton (b) drift paths of the projectile-like fragments as a function of time in the $^{138}\mathrm{Ce}+^{206}\mathrm{Pt}$ collisions with the $E_{\mathrm{c.m.}} = 526$ MeV at the initial orbital angular momentum $\ell = 100\,\hbar$.

Figure 6 shows the result of the TDHF calculations of the mean values of the neutron and proton numbers of the projectile-like fragments as a function of time in collision of $^{138}\mathrm{Ce}+^{206}\mathrm{Pt}$. In this system time evolution is more complex, but we can recognize a rapid drift during the time interval (200 – 400) fm/c along the iso-vector path toward the iso-scalar line and curving toward the asymmetry direction. As the system heats up the shell effects disappear, the system reverses direction, drifts along the symmetry toward the local minimum and almost reaches the minimum location of ^{136}Xe before it breaks-up at around 800 fm/c. By eliminating β from Eq. (22) and Eq. (23), we can derive an expression for α in terms of drift and diffusion coefficients. We use the drift information of the system $^{138}\mathrm{Ce}+^{206}\mathrm{Pt}$ to determine the average value of the iso-vector curvature parameter in the time interval from $t_1 = 210$ fm/c to $t_2 = 310$ fm/c. This time interval approximately correspond to the average taken over the maximum

overlap during the drift along the iso-vector path. The projection of this interval on the iso-vector line is indicated by a thick red line in Fig. (3). We evaluate the average value of the curvature α over this interval as,

$$\alpha = \frac{1}{\Delta t}\int_{t_1}^{t_2} d\tau \frac{1}{R_s(\tau)}\left(\frac{v_n(\tau)}{D_{NN}(\tau)}\sin\phi - \frac{v_p(\tau)}{D_{ZZ}(\tau)}\cos\phi\right) = 0.143\ . \quad (29)$$

Here, $\Delta t = t_2 - t_1$ and distance R_s is evaluated with $N_1(t)$, $Z_1(t)$ on the iso-vector path. The drift coefficients are determined from rate of change of the neutron and proton numbers in Fig. 6.

Since ^{138}Ce + ^{206}Pt system rapidly drifts toward the charge symmetry of the iso-scalar path, the asymmetry of the curvature parameter in the iso-vector direction does not have an important effect on the diffusion mechanism. Therefore, we neglect the asymmetry effect in the potential energy in the iso-vector direction. For determining the iso-scalar curvature parameter toward the symmetry direction $\beta_>$, we consider the associate system ^{142}Ba + ^{202}Hg. The charge asymmetry of nuclei ^{139}Te and ^{142}Ba have nearly the same value and are located on the iso-scalar path equal distance away from ^{136}Xe as indicated in Fig. 3. Similarly, charge asymmetry of nuclei ^{214}Po and ^{202}Hg have nearly the same value and are located close to the iso-scalar path equal distance away from ^{208}Pb. In order to save computing time, rather than carrying out the SMF calculations for ^{142}Ba + ^{202}Hg system, we estimate the iso-scalar curvature parameter toward the symmetry direction $\beta_>$, with the help of the $Q_{gg}-$value distribution along the iso-scalar path. The $Q_{gg}-$value of ^{130}Te + ^{214}Po system relative to ^{136}Xe + ^{208}Pb is $Q_{gg} = -16.2$ MeV. The associate system ^{142}Ba + ^{202}Hg has a $Q_{gg} = -2.99$ MeV value relative to ^{136}Xe + ^{208}Pb. We estimate the potential energy and therefore curvature parameter along symmetry direction with the ratio of the $Q_{gg}-$ values to give $\beta_> = \beta_<(2.99/16.2) = 0.023$. For a heavy di-nuclear system the rotational kinetic energy depends on the mass asymmetry variable in a smooth manner [36]. As a result, the effect of the rotational energy on the curvature parameters is very small, and hence in the orbital angular momentum range $\ell = (100-300)\,\hbar$ of the di-nuclear system ^{136}Xe + ^{208}Pb, the average value of the curvature parameters of the parabolic forms have approximately same magnitudes during the maximum overlap of the colliding nuclei. Furthermore, the curvature parameters should be proportional to the window area of the colliding nuclei for each orbital angular momentum. In order to take into account this window effect, we multiply the average values of the curvature parameters with a form factor $\beta_<^\ell(t) = \beta_< F_\ell(t)$, $\beta_>^\ell(t) = \beta_> F_\ell(t)$ and $\alpha_\ell(t) = \alpha F_\ell(t)$. We take this form factor to be the ratio of neutron diffusion coefficients of the ^{136}Xe + ^{208}Pb for each orbital angular momentum,

$$F_\ell(t) = D_\ell(t)/D_\ell(t_m)\ . \quad (30)$$

The ratio of the neutron diffusion coefficients provide a measure for the ratio of the window area at time t to the maximum window area at time t_m.

IV. FRAGMENT MASS DISTRIBUTION IN ^{136}Xe + ^{208}Pb

TABLE II. Asymptotic values of the variances, the co-variances of neutrons and protons, the mass dispersions in symmetric $\sigma_{AA}^>$ and in asymmetric $\sigma_{AA}^<$ directions, and the dispersion $\bar{\sigma}_{AA}$ of the middle Gauss functions for a set of initial orbital angular momentum in the interval $\ell = (100-300)\,\hbar$ in ^{136}Xe + ^{208}Pb collisions at $E_{\rm c.m.} = 526$ MeV.

$\ell_i\,(\hbar)$	$\sigma_{NN}^{2<}$	$\sigma_{ZZ}^{2<}$	$\sigma_{NZ}^{2<}$	$\sigma_{AA}^<$	$\sigma_{NN}^{2>}$	$\sigma_{ZZ}^{2>}$	$\sigma_{NZ}^{2>}$	$\sigma_{AA}^>$	$\bar{\sigma}_{AA}$
100	28.4	24.8	1.32	7.47	63.2	30.9	19.6	11.6	9.57
120	28.7	21.1	1.40	7.26	62.8	30.5	19.2	11.5	9.43
140	29.2	21.2	1.47	7.30	62.5	30.1	18.7	11.4	9.41
160	29.4	21.3	1.46	7.32	61.5	29.8	17.9	11.3	9.35
180	29.6	21.5	1.36	7.33	59.7	29.2	16.6	11.1	9.24
200	30.4	21.8	1.29	7.40	57.7	28.4	14.8	10.8	9.12
220	30.2	21.2	1.23	7.33	53.3	26.3	12.2	10.2	8.79
240	28.7	19.3	1.10	7.08	45.9	22.6	8.61	9.26	8.19
260	26.4	16.1	0.79	6.64	36.5	17.7	4.74	7.98	7.37
280	21.5	11.5	0.42	5.81	25.5	11.9	1.68	6.38	6.08
300	12.9	5.81	0.15	4.35	13.8	5.77	0.30	4.49	4.39

We determine the co-variances of the neutron $\sigma_{NN}^2(t)$ and the proton $\sigma_{ZZ}^2(t)$ variances and the mixed co-variance $\sigma_{NZ}^2(t)$ by solving the differential equations in Eqs. (12-14). Because of different curvature parameters in symmetric and asymmetric directions of the iso-scalar path, the variances and the co-variances have different values in symmetric and asymmetric directions. As an example, Fig. 7 shows the variances and the co-variance as a function of time for the initial orbital angular momentum $\ell = 100\hbar$. We find the dispersion of the mass number distributions using the expression $\sigma_{AA}^2(t) = \sigma_{NN}^2(t) + \sigma_{ZZ}^2(t) + 2\sigma_{NZ}^2(t)$. Table II shows the asymptotic values of the variances, the co-variances and the mass dispersions in symmetric $\sigma_{AA}^>$ and in asymmetric $\sigma_{AA}^<$ directions for a set of initial orbital angular momentum in the interval $\ell = (100-300)\,\hbar$

The mass number distributions in the asymmetry direction and the symmetry direction are determined by the Gauss functions

$$P_\ell^<(A-A_\ell) = \frac{1}{\sqrt{2\pi}}\frac{1}{\sigma_{AA}^<(\ell)} = \exp\left[-\frac{1}{2}\left(\frac{A-A_\ell}{\sigma_{AA}^<(\ell)}\right)^2\right], \quad (31)$$

and

$$P_\ell^>(A-A_\ell) = \frac{1}{\sqrt{2\pi}}\frac{1}{\sigma_{AA}^>(\ell)} = \exp\left[-\frac{1}{2}\left(\frac{A-A_\ell}{\sigma_{AA}^>(\ell)}\right)^2\right], \quad (32)$$

where, A_ℓ denotes the mean mass number of the projectile-like or the target-like fragments. Because of the asymmetric dispersions, these distribution functions do not match at the mean value of the mass number. In order to provide an approximate analytical description for the solution of the Langevin Eq. (10) we smoothly combine the left and right

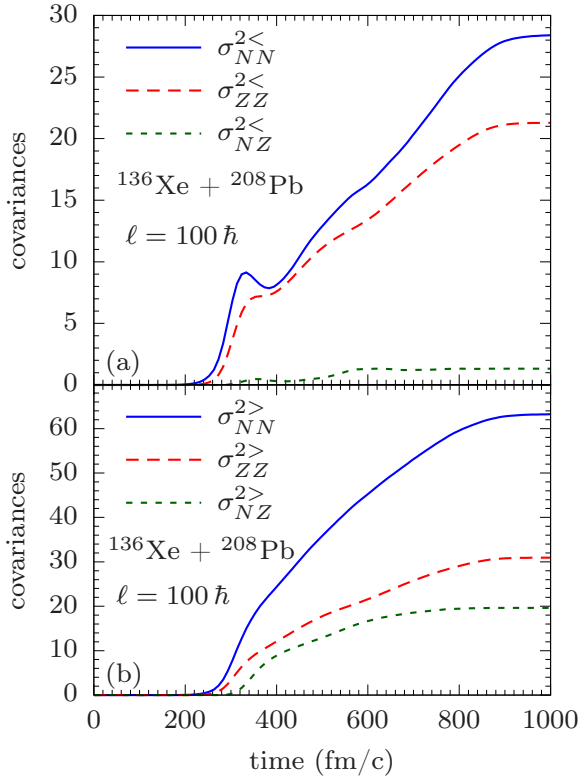

FIG. 7. (color online) The neutron, proton, and mixed variances as a function of time in the $^{136}\mathrm{Xe}+^{208}\mathrm{Pb}$ collisions with the $E_{\mathrm{c.m.}} =$ 526 MeV at the initial orbital angular momentum $\ell = 100\,\hbar$, towards asymmetry (a) and towards symmetry (b).

Gauss functions. We determine the right and left intersection points $A^0_\ell(R)$, $A^0_\ell(L)$ by matching the Gauss functions $P^<_\ell(A^0_\ell - A_\ell) = P^>_\ell(A_\ell - A^0_\ell) = \bar{P}_\ell$, and smoothly join the left and right Gauss functions between the intersection points by a middle Gauss function,

$$\bar{P}_\ell(A - A_\ell) = \bar{P}_\ell \exp\left[-\frac{1}{2}\left(\frac{A-A_\ell}{\bar{\sigma}_{AA}(\ell)}\right)^2 + \frac{1}{2}\left(\frac{\Delta A_\ell}{\bar{\sigma}_{AA}(\ell)}\right)^2\right], \tag{33}$$

where $\Delta A_\ell = A_\ell - A^0_\ell(L) = A^0_\ell(R) - A_\ell$. The dispersions of the middle Gauss functions are determined by requiring the entire distribution is normalized to one for each orbital angular momentum. This requirement is given by the integral relation,

$$\int_0^{\Delta A_\ell} \frac{1}{2} dA \left[P^<_\ell(A) + P^>_\ell(A)\right] = \int_0^{\Delta A_\ell} dA \bar{P}_\ell(A)\,. \tag{34}$$

Dispersions $\bar{\sigma}_{AA}(\ell)$ of the middle Gauss functions determined from this requirement are listed in the last column of Table II. The dispersion of the middle Gauss functions are approximately equal to the average values of the left and right dispersions, $\bar{\sigma}_{AA}(\ell) \approx \left(\sigma^<_{AA}(\ell) + \sigma^>_{AA}(\ell)\right)/2$. As a result, the middle Gauss functions describe nearly the average values of the left and the right Gauss functions in the intersection intervals, which have about $\Delta A_\ell \approx 8-10$ nucleons range from the mean values.

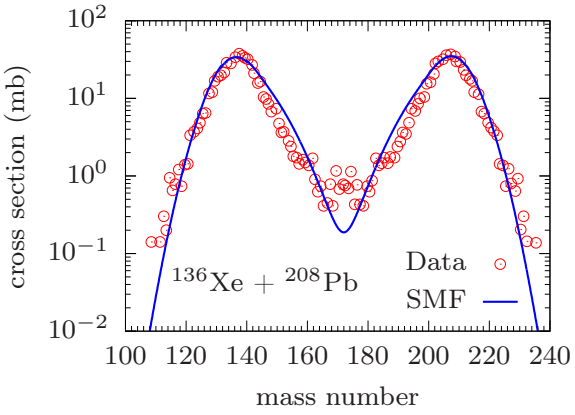

FIG. 8. (color online) Line shows mass number distribution of the primary fragments in collisions of $^{136}\mathrm{Xe}+^{208}\mathrm{Pb}$ system at $E_{\mathrm{c.m.}} =$ 526 MeV. Data is taken from [7].

We calculate the cross-section for production of a fragment with the mass number A using the standard expression,

$$\sigma(A) = \frac{\pi\hbar^2}{2\mu E_{\mathrm{c.m.}}} \sum_{\ell_{\min}}^{\ell_{\max}} (2\ell+1) P_\ell(A)\,, \tag{35}$$

where $P_\ell(A) = P_{1,\ell}(A) + P_{2,\ell}(A)$ is the probability distribution of the total fragments and the summation runs over from the $\ell_{\min} = 100\hbar$ to $\ell_{\max} = 300\hbar$. As shown in Table I, the total excitation energy of TDHF calculations at maximum $\ell_{\max} =$ 300 value is $E^* = 53.7$ MeV, which is nearly the same for the $TKE = 40.0$ MeV cut-off in the experimental fragment mass distribution in Fig. 8. Here, $P_{1,\ell}(A)$ and $P_{2,\ell}(A)$ denote the probability distribution functions of the projectile-like and the target-like fragments for the initial orbital angular momentum ℓ. The distribution functions of the projectile-like fragments and the target-like fragments are determined according to,

$$P_{1,\ell}(A) = \begin{cases} P^<_\ell(A - A_{1\ell}) & A \le A_{1\ell} - \Delta A_\ell \\ \bar{P}_\ell(A - A_{1\ell}) & A_{1\ell} - \Delta A_\ell \le A \le A_{1\ell} + \Delta A_\ell \\ P^>_\ell(A - A_{1\ell}) & A \ge A_{1\ell} + \Delta A_\ell \end{cases}, \tag{36}$$

and

$$P_{2,\ell}(A) = \begin{cases} P^<_\ell(A - A_{2\ell}) & A \le A_{2\ell} - \Delta A_\ell \\ \bar{P}_\ell(A - A_{2\ell}) & A_{2\ell} - \Delta A_\ell \le A \le A_{2\ell} + \Delta A_\ell \\ P^>_\ell(A - A_{2\ell}) & A \ge A_{2\ell} + \Delta A_\ell \end{cases}. \tag{37}$$

In these expressions $A_{1\ell}$ and $A_{2\ell}$ indicate the mean mass values of the projectile-like and the target-like primary fragments, respectively. We consider these distributions as averages over 20 angular momentum unit intervals and carry out the summation as follows,

$$\sigma(A) = \frac{\pi\hbar^2}{2\mu E_{\mathrm{c.m.}}} \sum_{n=0}^{n=10} 10 \times (2\ell_n + 1) P_{\ell_n}(A)\,. \tag{38}$$

Here, $\ell_n = 100 + 20 \times n$ denotes the average orbital angular momentum quantum number in the 20 unit intervals. Since the total probability $P_{\ell_n}(A)$ is normalized to two, the factor 10 appear rather than 20 in front of $(2\ell_n + 1)$. Fig. 8 presents a comparison of the calculated cross-section for the primary fragment production indicated by solid line in collision of the ^{136}Xe + ^{208}Pb system at $E_{\rm c.m.} = 526$ MeV and experimental cross-sections of Kozulin *et al.* [7] are indicated by circles. As seen from the first line of Table I, this range orbital angular momenta correspond to a limited laboratory angular range $25^\circ - 70^\circ$ for the detection of the binary fragments in coincidence. Production probabilities of the primary projectile-like and target-like fragments have mirror symmetry with different mean values. This feature of the probability distribution approximately takes into account for the fact that these fragments are detected in coincidence. Heavy primary target-like fragments may undergo sequential fission. In data presented in Fig. 6 of Ref. [7] these events are not included. The rate of these is estimated to be about 33%, which provides of a small fraction of the cross-section in the heavy target-like fragments side. On the other hand, all primary binary fragments production, in the orbital angular momentum range of $\ell = (100 - 300)\hbar$, is included in the calculations. We also add that a fraction of heavy target-like fragments, observed in the experimental angular range, which undergo sequential fission may originate from the orbital angular momentum smaller than $\ell = 100\hbar$, which is not included in the calculations

V. CONCLUSIONS

We carry out an investigation of mass distributions of the primary fragments produced in the collisions of the ^{136}Xe + ^{208}Pb system at $E_{\rm c.m.} = 526$ MeV. We calculate the mass distribution employing a quantal nucleon diffusion mechanism based on the SMF approach. The diffusion coefficients of neutrons and protons, which describes the fluctuation aspects of the mass distribution, are determined entirely in terms of the occupied single particle states of the TDHF equations and they do not involve any adjustable parameters other than the standard parameters of the effective Skyrme interaction. The evaluation of the transport coefficients in terms of the mean-field properties is consistent with the fundamental idea of the non-equilibrium fluctuation-dissipation theorem. The potential energy surface in the (N,Z)- plane has an important effect on the diffusion mechanism. As a result of the neutron shell closure of projectile and target with $N = 82$ and $N = 126$, respectively, and due the $Q_{gg}-$value distributions, the ^{136}Xe + ^{208}Pb system is located at a local potential energy minimum position in the $(N,Z)-$ plane. We parameterize the potential energy in the vicinity of this local minimum in terms of two parabolic forms along the iso-scalar and iso-vector directions. We determine the curvature parameters of the parabolic forms by carrying out the SMF calculations for two nearby systems ^{130}Te + ^{214}Po and ^{138}Ce + ^{206}Pt, and utilizing the $Q_{gg}-$value information of the systems ^{130}Te + ^{214}Po and ^{142}Ba + ^{202}Hg, which are located symmetrically on the $(N,Z)-$ plane along the iso-scalar direction. As seen in Fig. 8, the quantal diffusion calculations based on the SMF approach provides a very good description of the mass distribution of the primary fragments of data reported by the Kozulin *et al.* [7] without any adjustable parameters.

ACKNOWLEDGMENTS

S.A. gratefully acknowledges the IPN-Orsay and the Middle East Technical University for warm hospitality extended to him during his visits. S.A. also gratefully acknowledges useful discussions with D. Lacroix, and very much thankful to his wife F. Ayik for continuous support and encouragement. This work is supported in part by US DOE Grant Nos. DE-SC0015513 and DE-SC0013847, and in part TUBITAK Grant No. 117F109.

[1] C. H. Dasso, G. Pollarolo, and A. Winther, Systematics of Isotope Production with Radioactive Beams, Phys. Rev. Lett. **73**, 1907 (1994).

[2] L. Corradi, G. Pollarolo, and S. Szilner, Multinucleon transfer processes in heavy-ion reactions, J. Phys. G **36**, 113101 (2009).

[3] Kazuyuki Sekizawa, TDHF Theory and Its Extensions for the Multinucleon Transfer Reaction: A Mini Review, Front. Phys. **7**, 20 (2019).

[4] Valery Zagrebaev and Walter Greiner, Production of New Heavy Isotopes in Low–Energy Multinucleon Transfer Reactions, Phys. Rev. Lett. **101**, 122701 (2008).

[5] V. I. Zagrebaev and W. Greiner, Production of heavy and superheavy neutron-rich nuclei in transfer reactions, Phys. Rev. C **83**, 044618 (2011).

[6] V. I. Zagrebaev, A. V. Karpov, and W. Greiner, Possibilities for synthesis of new isotopes of superheavy elements in fusion reactions, Phys. Rev. C **85**, 014608 (2012).

[7] E. M. Kozulin, E. Vardaci, G. N. Knyazheva, A. A. Bogachev, S. N. Dmitriev, I. M. Itkis, M. G. Itkis, A. G. Knyazev, T. A. Loktev, K. V. Novikov, E. A. Razinkov, O. V. Rudakov, S. V. Smirnov, W. Trzaska, and V. I. Zagrebaev, Mass distributions of the system ^{136}Xe+ ^{208}Pb at laboratory energies around the Coulomb barrier: A candidate reaction for the production of neutron–rich nuclei at N=126, Phys. Rev. C **86**, 044611 (2012).

[8] Y. X. Watanabe, Y. H. Kim, S. C. Jeong, Y. Hirayama, N. Imai, H. Ishiyama, H. S. Jung, H. Miyatake, S. Choi, J. S. Song, E. Clement, G. de France, A. Navin, M. Rejmund, C. Schmitt, G. Pollarolo, L. Corradi, E. Fioretto, D. Montanari, M. Niikura, D. Suzuki, H. Nishibata, and J. Takatsu, Pathway for the Production of Neutron–Rich Isotopes around the $N = 126$ Shell Closure, Phys. Rev. Lett. **115**, 172503 (2015).

[9] V. V. Desai, W. Loveland, K. McCaleb, R. Yanez, G. Lane, S. S. Hota, M. W. Reed, H. Watanabe, S. Zhu, K. Auranen, A. D. Ayangeakaa, M. P. Carpenter, J. P. Greene, F. G. Kondev, D. Seweryniak, R. V. F. Janssens, and P. A. Copp, The ^{136}Xe + ^{198}Pt reaction: A test of models of multi-nucleon transfer reactions, Phys. Rev. C **99**, 044604 (2019).

[10] A. V. Karpov and V. V. Saiko, Modeling near-barrier collisions of heavy ions based on a Langevin-type approach, Phys. Rev. C **96**, 024618 (2017).

[11] V. V. Saiko and A. V. Karpov, Analysis of multinucleon transfer reactions with spherical and statically deformed nuclei using a Langevin-type approach, Phys. Rev. C **99**, 014613 (2019).

[12] J. W. Negele, The mean-field theory of nuclear-structure and dynamics, Rev. Mod. Phys. **54**, 913 (1982).

[13] C. Simenel, Nuclear quantum many-body dynamics, Eur. Phys. J. A **48**, 152 (2012).

[14] C. Simenel and A. S. Umar, Heavy–ion collisions and fission dynamics with the time–dependent Hartree-Fock theory and its extensions, Prog. Part. Nucl. Phys. **103**, 19 (2018).

[15] A. Wakhle, C. Simenel, D. J. Hinde, M. Dasgupta, M. Evers, D. H. Luong, R. du Rietz, and E. Williams, Interplay between Quantum Shells and Orientation in Quasifission, Phys. Rev. Lett. **113**, 182502 (2014).

[16] V. E. Oberacker, A. S. Umar, and C. Simenel, Dissipative dynamics in quasifission, Phys. Rev. C **90**, 054605 (2014).

[17] A. S. Umar, V. E. Oberacker, and C. Simenel, Shape evolution and collective dynamics of quasifission in the time-dependent Hartree-Fock approach, Phys. Rev. C **92**, 024621 (2015).

[18] A. S. Umar, V. E. Oberacker, and C. Simenel, Fusion and quasifission dynamics in the reactions ^{48}Ca + ^{249}Bk and ^{50}Ti + ^{249}Bk using a time-dependent Hartree-Fock approach, Phys. Rev. C **94**, 024605 (2016).

[19] K. Sekizawa and K. Yabana, Time-dependent Hartree-Fock calculations for multinucleon transfer and quasifission processes in the ^{64}Ni + ^{238}U reaction, Phys. Rev. C **93**, 054616 (2016).

[20] K. Sekizawa, Enhanced nucleon transfer in tip collisions of ^{238}U + ^{124}Sn, Phys. Rev. C **96**, 041601(R) (2017).

[21] Roger Balian and Marcel Véneroni, Fluctuations in a time-dependent mean-field approach, Phys. Lett. B **136**, 301 (1984).

[22] R. Balian and M. Véneroni, Time-dependent variational principle for the expectation value of an observable: Mean-field applications, Ann. Phys. **164**, 334 (1985).

[23] J. M. A. Broomfield and P. D. Stevenson, Mass dispersions from giant dipole resonances using the Balian-Véneroni variational approach, J. Phys. G **35**, 095102 (2008).

[24] J. M. A. Broomfield, *Calculations of Mass Distributions using the Balian-Véneroni Variational Approach*, Ph.D. thesis, University of Surrey (2009).

[25] C. Simenel, Particle-Number Fluctuations and Correlations in Transfer Reactions Obtained Using the Balian-Véneroni Variational Principle, Phys. Rev. Lett. **106**, 112502 (2011).

[26] E. Williams, K. Sekizawa, D. J. Hinde, C. Simenel, M. Dasgupta, I. P. Carter, K. J. Cook, D. Y. Jeung, S. D. McNeil, C. S. Palshetkar, D. C. Rafferty, K. Ramachandran, and A. Wakhle, Exploring Zeptosecond Quantum Equilibration Dynamics: From Deep-Inelastic to Fusion-Fission Outcomes in ^{58}Ni + ^{60}Ni Reactions, Phys. Rev. Lett. **120**, 022501 (2018).

[27] S. Ayik, A stochastic mean-field approach for nuclear dynamics, Phys. Lett. B **658**, 174 (2008).

[28] D. Lacroix and S. Ayik, Stochastic quantum dynamics beyond mean field, Eur. Phys. J. A **50**, 95 (2014).

[29] C. W. Gardiner, *Quantum Noise* (Springer–Verlag, Berlin, 1991).

[30] U. Weiss, *Quantum Dissipative Systems*, 2nd ed. (World Scientific, Singapore, 1999).

[31] S. Ayik, B. Yilmaz, O. Yilmaz, A. S. Umar, and G. Turan, Multinucleon transfer in central collisions of ^{238}U + ^{238}U, Phys. Rev. C **96**, 024611 (2017).

[32] S. Ayik, B. Yilmaz, O. Yilmaz, and A. S. Umar, Quantal diffusion description of multinucleon transfers in heavy–ion collisions, Phys. Rev. C **97**, 054618 (2018).

[33] B. Yilmaz, S. Ayik, O. Yilmaz, and A. S. Umar, Multinucleon transfer in ^{58}Ni + ^{60}Ni and ^{60}Ni + ^{60}Ni in a stochastic mean-field approach, Phys. Rev. C **98**, 034604 (2018).

[34] A. S. Umar and V. E. Oberacker, Three-dimensional unrestricted time-dependent Hartree-Fock fusion calculations using the full Skyrme interaction, Phys. Rev. C **73**, 054607 (2006).

[35] W. U. Schröder, J. R. Huizenga, and J. Randrup, Correlated mass and charge transport induced by statistical nucleon exchange in damped nuclear reactions, Phys. Lett. B **98**, 355 (1981).

[36] A. C. Merchant and W. Nörenberg, Microscopic transport theory of heavy-ion collisions, Z. Phys. A **308**, 315 (1982).

[37] Hannes Risken and Till Frank, *The Fokker–Planck Equation* (Springer–Verlag, Berlin, 1996).